RSC Advances

PAPER

View Article Online
View Journal | View Issue

Cite this: *RSC Adv.*, 2023, **13**, 19856

Entropy stabilized cubic $Li_7La_3Zr_2O_{12}$ with reduced lithium diffusion activation energy: studied using solid-state NMR spectroscopy†

Juntian Fan,[ab] Tao Wang,[b] Craig A. Bridges,[b] Albina Y. Borisevich,[c] Carlos A. Steren,[a] Pengzhen Li,[d] Bishnu P. Thapaliya,[b] Chi-Linh Do-Thanh,[a] Zhenzhen Yang,[b] Yating Yuan[b] and Sheng Dai *[ab]

Received 3rd April 2023
Accepted 14th June 2023

DOI: 10.1039/d3ra02206d

rsc.li/rsc-advances

Stabilizing cubic polymorph of $Li_7La_3Zr_2O_{12}$ at low temperatures is challenging and currently limited to mono- or dual-ion doping with aliovalent ions. Herein, a high-entropy strategy at the Zr sites was deployed to stabilize the cubic phase and lower the lithium diffusion activation energy, evident from the static ^{7}Li and MAS ^{6}Li NMR spectra.

Solid-state electrolytes, characterized by superior thermal and mechanical stability, high safety, *etc.*, are the most crucial component for next generation alkali-ion batteries.[1,2] Among diverse solid-state electrolytes including inorganic and polymer electrolytes, garnet electrolyte $Li_7La_3Zr_2O_{12}$ (LLZO) has drawn a great deal of scientific attention, due to its high ionic conductivity, wide potential window, and potential feasibility in lithium-metal batteries after Murugan *et al.*'s initial investigations in 2007.[3,4] Among the two different phases of garnet LLZO (tetragonal and cubic phases), the cubic phase exhibits a two-orders of magnitude higher lithium ion conductivity than the tetragonal phase as it has more available migration sites for lithium diffusion.[5] Specifically, Li-ions and Li-ion vacancies of the cubic LLZO form a percolative network of tetrahedral (24d) and octahedral sites (48g/96h) for lithium migration through a three-dimensional framework composed of edge-sharing ZrO_6 octahedra and LaO_8 dodecahedra. However, the cubic phase is unstable at low temperatures (*e.g.* room temperature) and easily transforms into a tetragonal phase, resulting in decreased ionic conductivity.[6] Therefore, one of the key challenges with deploying LLZO in lithium-ion batteries is stabilizing the cubic polymorphs at room temperature to increase their ionic conductivity. It has been found that the formation of lithium vacancies using the aliovalent doping strategy at Li sites by Al, Ga, Fe or at Zr sites by Nb, Ta, Cr, Bi, W, Mo, Sb, *etc.*, is one of the most effective methods for inhibiting change in crystal structure and stabilizing cubic phases.[7–10]

Meanwhile, it has been reported that increased configurational entropy contributes to the phase stability of functional materials in accordance with the second law of thermodynamics.[11] High-entropy materials are a unique class of functional materials that contain five or more elements in near-equiatomic ratios within a single-phase solid solution.[12] In addition, maximized configurational entropy could induce local disorder, thus creating overlapping site energy distributions for charge-carrying ions, thus boosting the ionic mobility of the electrode materials (*e.g.* high-entropy layered O_3-type cathodes $NaMO_2$, high-entropy metal fluorides, *etc.*) or the electrolyte materials (*e.g.* high-entropy lithium superionic conductor, high-entropy sodium NASICON) to achieve enhanced rate performance or boosted ionic conductivity for energy storage fields.[13–15] Herein, the high-entropy strategy utilizing five metal cations to reside at the Zr site was applied to stabilize the cubic garnet structure and lower the lithium diffusion activation energy, in which the five metals were selected from previously reported traditional single-metal doped LLZO. Dopants at Zr^{4+} sites were selected since they will not reside on the Li sublattice and retard lithium diffusion in contrast to dopants on the Li site (*e.g.*, Al^{3+}).[16] To select the most important metal elements from the tens of elements that have been reported, machine learning was deployed to explore the correlation between the metal ions and the ionic conductivity, from which the Nb^{5+}, Ta^{5+} and W^{6+} were selected to be doped at Zr^{4+} as these three metal elements exhibited a large impact on the final ionic conductivity. Moreover, the Sn^{4+} or Hf^{4+} which possesses the same valence as Zr^{4+} was also chosen to help sustain the structure and simultaneously improve the degree of disorder. Therefore, the HE-LLZO materials $Li_{5.4}La_3(Zr_{0.4}Hf_{0.4}Nb_{0.4}Ta_{0.4}W_{0.4})O_{12}$ and $Li_{5.4}La_3(Zr_{0.4}Sn_{0.4}Nb_{0.4}Ta_{0.4}W_{0.4})O_{12}$, were synthesized and

[a]*Department of Chemistry, University of Tennessee, Knoxville, TN 37996, USA*
[b]*Chemical Sciences Division, Oak Ridge National Laboratory, Oak Ridge, 37831, USA. E-mail: dais@ornl.gov*
[c]*Center for Nanophase Materials Sciences, Oak Ridge National Laboratory, Oak Ridge, 37831, USA*
[d]*Department of Agricultural and Resource Economics, University of Tennessee, Knoxville, TN 37996, USA*

† Electronic supplementary information (ESI) available. See DOI: https://doi.org/10.1039/d3ra02206d

characterized. The HE-LLZOs show improved stability at low temperatures and lower lithium diffusion activation energies (0.361 eV for Hf-containing HE-LLZO and 0.393 eV for Sn-containing LLZO) compared to conventional LLZOs with only Zr at the M site (0.474 eV) from the static variable temperature ^{7}Li NMR analysis. In addition, to unveil the reason for the faster lithium dynamics in Hf-containing HE-LLZO than Sn-containing HE-LLZO, an analysis of MAS ^{6}Li NMR spectra was performed, which indicates that the higher Li concentration at the 96h octahedral site (55.09% *vs.* 33.73%) as well as lower Li concentration at the 24d (7.53% *vs.* 22.94%) in Hf-containing HE-LLZO account for the fast lithium dynamics.

It is widely recognized that the dopant plays a crucial role in determining the lithium diffusion activities of LLZO, and a plethora of elements have been reported to serve as dopants. However, the large number of reported elements introduces a vast array of potential doping strategies and combinations when designing high-entropy LLZO. For instance, selecting just 5 elements from a pool of 10 dopants results in 252 possible combinations, which can be both time-consuming and expensive to explore. To address this issue and identify the most appropriate and important dopants, machine learning is a promising solution that can accelerate materials discovery by leveraging existing materials data rather than relying on manual trial and error. Additionally, machine learning offers the advantage of optimizing complex systems with multiple interdependent variables. As such, machine learning was utilized as a first step to identify the most critical elements for high-entropy LLZO. As shown in Fig. S1,† six data mining strategies including ordinary least squares (OLS), K nearest-neighbor (KNN), ridge regression, principal components regression (PCR), partial least squares regression (PLS), and random forest (RF) were deployed to explore any probable relationships or trends between various metal ions and the ionic conductivity for helping select appropriate metal ions on the Zr site of the LLZO. Based on the radar charts (see ESI† for details), it was determined that Nb, W, and Ta are vital for determining lithium diffusion properties, and were therefore chosen to reside at the Zr sites, while Sn or Hf, which have similar radii and valences as Zr, were also selected to help maintain the structure and increase the disorder of the high-entropy garnet phase. It should be noted that although Hf is more expensive than Zr, it remains a promising dopant for LLZO. Zr precursors often contain Hf impurities due to the presence of 1–3% hafnium in natural zirconium ores. As a result, if Hf is chosen as the dopant, Zr precursors with Hf contamination could be selected, which are almost 75% cheaper than pure Zr precursors.[17]

To demonstrate the feasibility of the construction of high-entropy LLZOs, a non-aqueous sol–gel chemistry process based on citric acid chelation of metal chlorides or metal nitrides was deployed (details in ESI†).[18] This method can not only bypass the hydrolysis of the metal ions but can also provide the products with superior compositional homogeneity at lower temperatures with simple laboratory equipment compared to the traditional solid-state reactions, making it a promising synthesis method for high entropy materials.[19,20] After evaporating the organic solvents, the garnet electrolytes including the single-metal LLZO ($Li_7La_3Zr_2O_{12}$) and high-entropy counterparts (HE-LLZOs) were obtained by calcinating the precursors at 700 °C for 12 hours. Then, powder X-ray diffraction (PXRD) was used to determine the crystalline structure and phase purity of the as-synthesized LLZO and HE-LLZO. As shown in Fig. 1, the single-metal $Li_7La_3Zr_2O_{12}$ stored at 200 °C exhibited the high Li^+ conductive cubic phase, as evident by the XRD peaks being well indexed with the cubic structure $Li_5La_3Nb_2O_{12}$ (PDF45-0109). However, after cooling down to room temperature for several hours, the single-metal $Li_7La_3Zr_2O_{12}$ exhibited the combination of cubic phase and the tetragonal phase, as evidenced by the some of XRD peaks splitting into "doublets", which indicates that the relatively low Li^+ conductive tetragonal phase was more thermodynamically stable at low temperature and thus the transformation from cubic phase to tetragonal phase occurs.[21] As a comparison, both the diffraction peaks of the HE-LLZOs powders exhibited the desirable cubic phase at room temperature, indicating that the cubic garnet framework can accommodate aliovalent ions of different sizes at the Zr site without modifying the symmetry. A possible explanation for this observation lies in the fact that a high configurational entropy, as predicted by the Gibbs free energy equation ($G = H - TS$), can lead to a negative Gibbs free energy change, allowing for spontaneous processes to occur and overcome lattice mismatch caused by differences in metal ion sizes.[22,23] Specifically, due to the incorporation of five different metal ions, the configurational entropy was enhanced from 0R to 1.60R (R is gas constant, 0.013 kJ mol^{-1} K^{-1}), which in turn enhanced the stability of the cubic phase at the low temperature (The calculation for the configurational entropy is shown in the ESI†). Additionally, the XRD peak shifts were analyzed in order to further demonstrate the high-entropy structure. To be specific, among the six metal ions used in this work, Zr^{4+} has the largest radius of 0.72 Å in the high-spin state with a coordination number of six, whereas W^{6+} has the smallest radius of 0.6 Å. In addition, the radius of Sn^{4+}, Hf^{4+}, Nb^{5+} and Ta^{5+} is 0.69, 0.71, 0.64, 0.64 Å, respectively. The diffraction peaks of the HE-LLZOs shift to the right compared with those of $Li_7La_3Zr_2O_{12}$, indicating a lattice shrinkage due to the partial replacement of Zr^{4+} by smaller metal ions. Moreover, there is a direct relationship

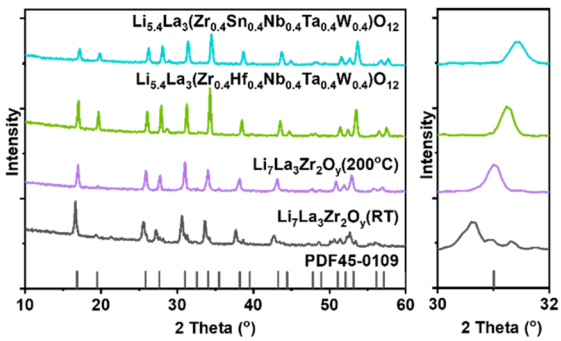

Fig. 1 PXRD patterns of as-synthesized $Li_7La_3Zr_2O_{12}$ stored at room temperature and 200 °C, and HE-LLZOs stored at room temperature.

between the degree of the right shift and the metal ions in the HE-LLZO. For example, $Li_{5.4}La_3(Zr_{0.4}Hf_{0.4}Nb_{0.4}Ta_{0.4}W_{0.4})O_{12}$ showed slightly left-shifted diffraction peaks compared to those of $Li_{5.4}La_3(Zr_{0.4}Sn_{0.4}Nb_{0.4}Ta_{0.4}W_{0.4})O_{12}$ due to the larger radius of Hf^{4+} than Sn^{4+}. Moreover, the Rietveld refinement analysis of XRD was also performed to confirm the similar results. The unit-cell parameters ($a = b = c$), cell volume (V), residual of least-squares refinement (R_p), weighted profile residual (R_{wp}) of different cubic garnets were calculated and shown in Fig. S2–S4 and Table S1,† which showed that the lattice parameters and cell volume decreased with replacing Zr by smaller metal ions, demonstrating that the metal ions were uniformly distributed at the Zr^{4+} site.

To better understand the structures of the HE-LLZOs, energy dispersive X-ray spectroscopy (EDX), scanning electron microscopy (SEM), and EDX mapping were used to determine their metal compositions, morphologies, and element distributions. Taking $Li_{5.4}La_3(Zr_{0.4}Hf_{0.4}Nb_{0.4}Ta_{0.4}W_{0.4})O_{12}$ as a representative, the EDX spectrum (Fig. S5†) showed that the atomic ratio of Zr : Hf : Nb : Ta : W is 0.207 : 0.183 : 0.198 : 0.242 : 0.170, indicating a near equiatomic ratio of different metal ions at Zr site. In addition, the EDX mapping showed that different metal elements (Zr, Hf, Nb, Ta, W) are uniformly distributed across the particles (Fig. 2). In combination with the EDX spectrum, uniform element distribution, and single-phase XRD pattern, the as-synthesized $Li_{5.4}La_3(Zr_{0.4}Hf_{0.4}Nb_{0.4}Ta_{0.4}W_{0.4})O_{12}$ indeed exhibited a high-entropy structure. Similarly, cubic-phase $Li_{5.4}La_3(Zr_{0.4}Sn_{0.4}Nb_{0.4}Ta_{0.4}W_{0.4})O_{12}$, with uniform element distributions and equiatomic ratio of different dopants (Fig. S6 and S7†), is also HE-LLZO.

After demonstrating the high-entropy structure, high-resolution scanning transmission electron microscopy (STEM) was used to demonstrate the structural stability of HE-LLZOs at room temperature. Fig. 3 shows high-angle annular dark field (HAADF) STEM images and diffractogram of HAADF of single-metal LLZO and HE-LLZO ($Li_{5.4}La_3(Zr_{0.4}Hf_{0.4}Nb_{0.4}Ta_{0.4}W_{0.4})O_{12}$) stored at room temperature. For single-metal LLZO, lattice spacings of 2.6 and 3.3 Å were observed in Fig. 3A, corresponding to the (422) and (400) planes of the tetragonal phase. Moreover, additional lattice spacings of 2.8 and 2.9 Å were

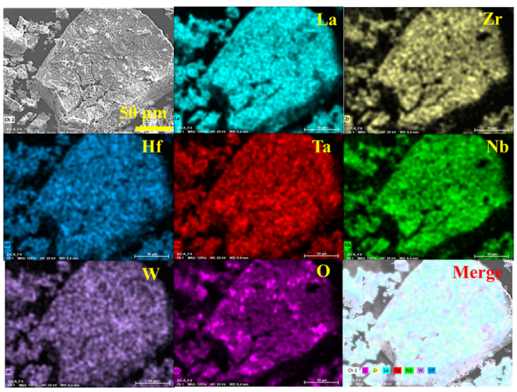

Fig. 2 EDX mapping of the high entropy $Li_{5.4}La_3(Zr_{0.4}Hf_{0.4}Nb_{0.4}Ta_{0.4}W_{0.4})O_{12}$.

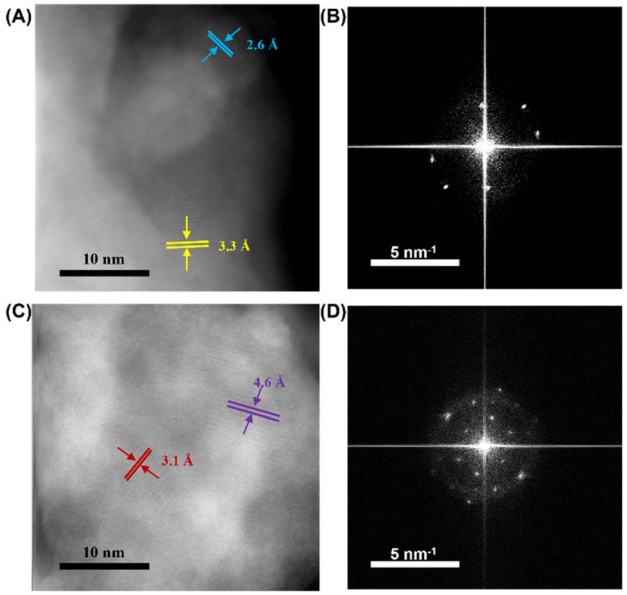

Fig. 3 Single-metal LLZO: (A) high-resolution HAADF-STEM image; (B) diffractogram of the image in panel (A). HE-LLZO ($Li_{5.4}La_3(Zr_{0.4}Hf_{0.4}Nb_{0.4}Ta_{0.4}W_{0.4})O_{12}$): (C) high-resolution HAADF-STEM image; (D) diffractogram of the image in panel (C).

observed in Fig. 3B, which were aligned with the peak split of (420) into (402) and (420) observed in the XRD figures (Fig. 1), providing further evidence for the existence of the tetragonal phase. HE-LLZO stored at room temperature displayed lattice spacings of 3.1, 4.6 Å, corresponding to 3.2 Å for (400) and 4.6 Å for (220) of standard cubic phase (Fig. 3C). Supplementally, diffractogram showed another characteristic lattice spacing of 5.3 Å for (211) plane (Fig. 3D), further supporting the cubic stability of HE-LLZOs.

To understand the lithium diffusion behavior of the as-synthesized HE-LLZOs, NMR line spectra of the quadrupole ^7Li nucleus (spin quantum number $I = 3/2$) were collected at a Larmor frequency of $\omega_0/2\pi = 155.38$ MHz. Solid-state NMR techniques were chosen herein due to their capability to detect the local structure and ion dynamics of solid electrolyte at their atomic level.[24] Additionally, solid-state NMR provides the advantage of analyzing solid electrolytes in their native state, allowing for accurate ion dynamics without being influenced by external factors like the quality of the solid-state electrolyte (*e.g.*, density of electrolyte pellets).[24] To be specific, because the line-shapes of the spectra are highly dependent on both local and long-range Li ion diffusion processes, they can provide the lithium hopping information.[25] In general, samples with higher lithium diffusion dynamics would have narrower ^7Li signals. It is therefore possible to obtain preliminary information about Li ion dynamics by comparing line-shapes for samples with different compositions at the same temperature. As shown in Fig. 4A, one symmetric peak with a slightly different linewidth was observed for all samples at the same temperature of 30 °C, and the HE-LLZOs exhibited a much smaller full width at half maximum (FWHM) than LLZO, indicating higher lithium ionic conductivity of the HE-LLZOs. Additionally, the FWHMs of the

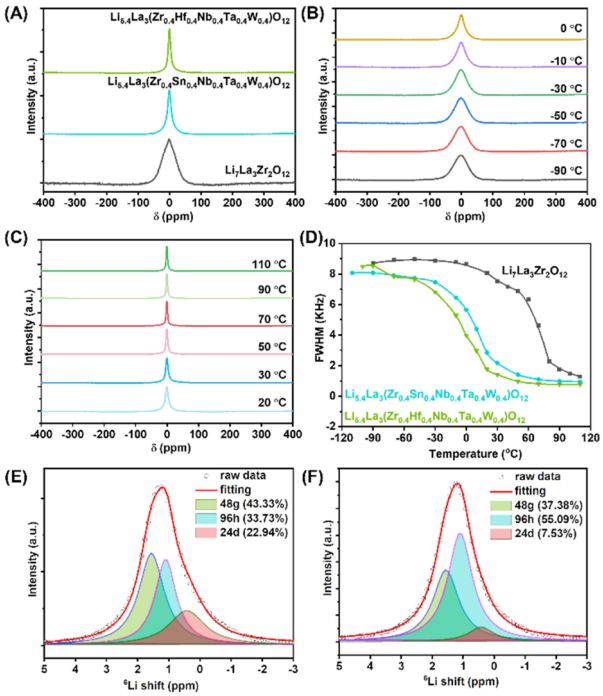

Fig. 4 (A) Static ^{7}Li NMR spectra for single-metal LLZO and HE-LLZOs at 30 °C. (B and C) Temperature-variable static ^{7}Li NMR spectra for HE-LLZO: $Li_{5.4}La_3(Zr_{0.4}Hf_{0.4}Nb_{0.4}Ta_{0.4}W_{0.4})O_{12}$. (D) FWHM linewidths δ *versus* temperature according to the results of temperature-variable static ^{7}Li NMR tests (the peaks were re-scaled to show similar intensities). (E) Peak fitting of MAS ^{6}Li NMR spectra for HE-LLZO: $Li_{5.4}La_3(Zr_{0.4}Sn_{0.4}Nb_{0.4}Ta_{0.4}W_{0.4})O_{12}$ by DMFIT. (F) Peak fitting of MAS ^{6}Li NMR spectra for HE-LLZO: $Li_{5.4}La_3(Zr_{0.4}Hf_{0.4}Nb_{0.4}Ta_{0.4}W_{0.4})O_{12}$ by DMFIT.

HE-LLZOs differ. The FWHM of $Li_{5.4}La_3(Zr_{0.4}Hf_{0.4}Nb_{0.4}Ta_{0.4}W_{0.4})O_{12}$ was 1411 Hz while $Li_{5.4}La_3(Zr_{0.4}Sn_{0.4}Nb_{0.4}Ta_{0.4}W_{0.4})O_{12}$ was 2171 Hz, showing that $Li_{5.4}La_3(Zr_{0.4}Hf_{0.4}Nb_{0.4}Ta_{0.4}W_{0.4})O_{12}$ has a superior ionic diffusion than $Li_{5.4}La_3(Zr_{0.4}Sn_{0.4}Nb_{0.4}Ta_{0.4}W_{0.4})O_{12}$. Moreover, the ^{7}Li NMR linewidth at various temperatures was also collected to further investigate the lithium diffusion activation energy. As shown in Fig. 4B and C and S8,† the NMR linewidth as a function of temperature for all the samples display a typical motional narrowing curve, with broadened spectra at low temperature due to lithium ion dipolar interactions. The observed narrow spectra at high temperature are due to the averaging of ^{7}Li–7Li dipole–dipole interactions.[25] The estimation of the activation energy of the Li diffusion process can be performed by employing the empirical equation of Waugh and Fedin: $E_a = 1.617 \times 10^{-3} \times T_c/K$, with T_c denoting the onset temperature of motional narrowing.[25] As shown in Fig. 4D, the onset temperature of line narrowing for LLZO, $Li_{5.4}La_3(Zr_{0.4}Hf_{0.4}Nb_{0.4}Ta_{0.4}W_{0.4})O_{12}$ and $Li_{5.4}La_3(Zr_{0.4}Sn_{0.4}Nb_{0.4}Ta_{0.4}W_{0.4})O_{12}$ were around 293.15 K, 223.15 K, and 243.15 K, respectively, corresponding to the diffusion activation energies of 0.474 eV, 0.361 eV and 0.393 eV, which clearly showed the fast lithium ion diffusion of the HE-LLZOs over the LLZO counterparts. Moreover, the $Li_{5.4}La_3(Zr_{0.4}Hf_{0.4}Nb_{0.4}Ta_{0.4}W_{0.4})O_{12}$ showed lower lithium diffusion activation energy than $Li_{5.4}La_3(Zr_{0.4}Sn_{0.4}Nb_{0.4}Ta_{0.4}W_{0.4})O_{12}$. This difference can be explained taking into account that the distribution of lithium ions along tetrahedral (24d) or octahedral sites (48g/96h) significantly influences the mobility of lithium ions, thus influencing the ionic conductivity of the garnet electrolytes.[26] Specifically, the ionic conductivity can be enhanced by increasing the lithium amount at the 96h site and reducing the lithium amount along the 24d site.[27–30] To further investigate ion conductivity mechanism behind these two high-entropy electrolytes, the distribution of lithium ions on the tetrahedral and octahedral sites was explored by ^{6}Li MAS NMR. ^{6}Li was chosen because it has a smaller quadrupole moment compared to ^{7}Li and thus enhanced resolution. As shown in Fig. 4E and F, the HE-LLZOs displayed three distinct Li environments, corresponding to Li^+ occupying the 24d tetrahedral (0.4 ppm), 48g octahedral (1.6 ppm), and 96h octahedral (1.1 ppm) sites, respectively.[31] For deconvolution, DMFIT was used to quantify each component, which showed that while the integration of the 48g site remained similar for the two HE-LLZOs, the integrations of 24d and 96h differed, with $Li_{5.4}La_3(Zr_{0.4}Hf_{0.4}Nb_{0.4}Ta_{0.4}W_{0.4})O_{12}$ exhibiting a higher content of 96h (55.09%) and a lower content of 24d (7.53%), compared to $Li_{5.4}La_3(Zr_{0.4}Sn_{0.4}Nb_{0.4}Ta_{0.4}W_{0.4})O_{12}$ (33.73% for 96h and 22.94% for 24d). As stated before, higher 96h and lower 24d lithium concentrations were beneficial to lithium diffusion, which explained the lower lithium diffusion activation energy of $Li_{5.4}La_3(Zr_{0.4}Hf_{0.4}Nb_{0.4}Ta_{0.4}W_{0.4})O_{12}$.

To intuitively understand the advantage of the high-entropy strategy, the electrochemical impedance spectroscopy (EIS) test was conducted to obtain the ionic conductivity of the single-metal LLZO and HE-LLZO. It should be noted that unlike solid-state NMR, the EIS test results are highly influenced by the pellet quality, which is dependent on factors such as sintering temperature, sintering atmosphere, press mode (cold press or hot press), and the presence of sintering aid agents. For instance, increasing the sintering temperature from 1100 °C to 1180 °C has been shown to increase the ionic conductivity of Al-doped LLZO (Al content: 0.1 mol) by approximately 10 times.[32] Typically, sintering temperatures above 1000 °C are used to achieve high pellet density and thus better ionic conductivity. However, LLZOs synthesized by sol–gel method in this work utilized a low-temperature process, with a sintering temperature of only 700 °C. Higher temperature would lead to lithium loss and the formation of another phase of $La_2Zr_2O_7$ (as depicted in Fig. S9†). As a result, cold pressing followed by a 700 °C calcination for 10 hours was employed to prepare pellets. To measure the ionic conductivity of the resulting pellets, gold was sputtered on both sides, acting as blocking electrodes. The EIS test was conducted at room temperature, ranging from 1 Hz to 7 MHz, and the results are presented in Fig. 5A and B. Furthermore, the Nyquist plots were fitted using an equivalent circuit,[33] which mainly comprises two resistors in parallel with constant phase elements (CPE) where the resistors correspond to ionic conduction within the grains (R_{bulk}) and the grain boundaries (R_{gb}), while the CPEs account for the material's inhomogeneity and imperfections in physical properties (Fig. 5C).[34,35] Based on the equivalent circuit results, the total resistance (R_{total}) of single-metal LLZO and $Li_{5.4}La_3(Zr_{0.4}Hf_{0.4}Nb_{0.4}Ta_{0.4}W_{0.4})O_{12}$ was measured at 26 660 Ω and 5085 Ω,

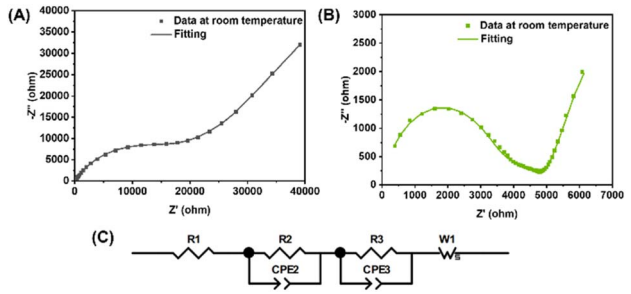

Fig. 5 (A) Nyquist plot of $Li_7La_3Zr_2O_{12}$. (B) Nyquist plot of $Li_{5.4}La_3(Zr_{0.4}Hf_{0.4}Nb_{0.4}Ta_{0.4}W_{0.4})O_{12}$. (C) Equivalent circuit.

respectively. Utilizing the equation $\sigma = l/(A \times R)$, where σ is the total ionic conductivity, l is the pellet thickness, and A is the electrode area, the total ionic conductivity for single-metal LLZO was determined to be 3.2×10^{-6} S cm^{-1}, which is comparable to sol–gel-derived LLZO reported in the literature.[36,37] In comparison, $Li_{5.4}La_3(Zr_{0.4}Hf_{0.4}Nb_{0.4}Ta_{0.4}W_{0.4})O_{12}$ exhibited a total ionic conductivity of 1.7×10^{-5} S cm^{-1}, highlighting the improved ionic conductivity achieved through the high-entropy strategy.

In conclusion, entropy-stabilized cubic $Li_7La_3Zr_2O_{12}$ with reduced lithium diffusion activation energy by incorporation of five different dopants at the Zr site has been achieved in this work. The aliovalent ion dopants including Nb^{5+}, Ta^{5+}, and W^{6+} were determined by comprehensively considering their influence on the ionic conductivity with the aid of machine learning. In addition, Sn^{4+} or Hf^{4+} was also selected to boost the configurational entropy without compromising the valence change at Zr^{4+} site. This high-entropy strategy for LLZO has been demonstrated to be capable of stabilizing its cubic phase at low temperatures. Furthermore, static ^{7}Li NMR and MAS ^{6}Li NMR spectra were used to analyze lithium diffusion, which indicated that entropy-driven cubic-phase garnets displayed superior lithium diffusion dynamics over undoped LLZOs, validating the enhanced configurational entropy-boosted lithium diffusion theory. In summary, the current study indicates that a high entropy strategy by incorporating five or more metal elements in a single-phase solid solution can be utilized for the most promising solid electrolyte (garnet solid electrolyte), which will not only enhance the cubic phase stability at low temperature and lower the lithium-ion diffusion activation energy of the LLZO, but also offer new concepts and compelling evidence of high entropy strategy to enhance lithium diffusion performance for other categories of solid electrolytes.

Conflicts of interest

There are no conflicts to declare.

Acknowledgements

This work was supported by the U.S. Department of Energy, Office of Science, Basic Energy Sciences, Materials Sciences and Engineering Division.

Notes and references

1 T. Famprikis, P. Canepa, J. A. Dawson, M. S. Islam and C. Masquelier, *Nat. Mater.*, 2019, **18**, 1278–1291.
2 A. Manthiram, X. Yu and S. Wang, *Nat. Rev. Mater.*, 2017, **2**, 16103.
3 R. Murugan, V. Thangadurai and W. Weppner, *Angew. Chem., Int. Ed.*, 2007, **46**, 7778–7781.
4 X.-B. Cheng, C.-Z. Zhao, Y.-X. Yao, H. Liu and Q. Zhang, *Chem*, 2019, **5**, 74–96.
5 Q. Liu, Z. Geng, C. Han, Y. Fu, S. Li, Y.-b. He, F. Kang and B. Li, *J. Power Sources*, 2018, **389**, 120–134.
6 Y. Zhang, F. Chen, R. Tu, Q. Shen and L. Zhang, *J. Power Sources*, 2014, **268**, 960–964.
7 X. Xiang, F. Chen, W. Yang, J. Yang, X. Ma, D. Chen, K. Su, Q. Shen and L. Zhang, *J. Am. Ceram. Soc.*, 2020, **103**, 2483–2490.
8 Y. Li, Z. Wang, Y. Cao, F. Du, C. Chen, Z. Cui and X. Guo, *Electrochim. Acta*, 2015, **180**, 37–42.
9 X. Zhou, L. Huang, O. Elkedim, Y. Xie, Y. Luo, Q. Chen, Y. Zhang and Y. Chen, *J. Alloys Compd.*, 2022, **891**, 161906.
10 J. Han and J. C. Kim, *Chem. Commun.*, 2020, **56**, 15197–15200.
11 S.-K. Jung, H. Gwon, H. Kim, G. Yoon, D. Shin, J. Hong, C. Jung and J.-S. Kim, *Nat. Commun.*, 2022, **13**, 7638.
12 S. Dai, *ChemSusChem*, 2020, **13**, 1915–1917.
13 Y. Zeng, B. Ouyang, J. Liu, Y. W. Byeon, Z. Cai, L. J. Miara, Y. Wang and G. Ceder, *Science*, 2022, **378**, 1320–1324.
14 C. Zhao, F. Ding, Y. Lu, L. Chen and Y.-S. Hu, *Angew. Chem., Int. Ed.*, 2020, **59**, 264–269.
15 Y. Y. Cui, P. A. Sukkurji, K. Wang, R. Azmi, A. M. Nunn, H. Hahn, B. Breitung, Y. Y. Ting, P. M. Kowalski, P. Kaghazchi, Q. S. Wang, S. Schweidler and M. Botros, *J. Energy Chem.*, 2022, **72**, 342–351.
16 D. O. Shin, K. Oh, K. M. Kim, K.-Y. Park, B. Lee, Y.-G. Lee and K. Kang, *Sci. Rep.*, 2015, **5**, 18053.
17 M. Mann, M. Küpers, G. Häuschen, M. Finsterbusch, D. Fattakhova-Rohlfing and O. Guillon, *Ionics*, 2022, **28**, 53–62.
18 C. Tian, X. Zhu, C. W. Abney, X. Liu, G. S. Foo, Z. Wu, M. Li, H. M. Meyer III, S. Brown, S. M. Mahurin, S. Wu, S.-Z. Yang, J. Liu and S. Dai, *ACS Catal.*, 2017, **7**, 3388–3393.
19 M. Niederberger, *Acc. Chem. Res.*, 2007, **40**, 793–800.
20 G. Wang, J. Qin, Y. Feng, B. Feng, S. Yang, Z. Wang, Y. Zhao and J. Wei, *ACS Appl. Mater. Interfaces*, 2020, **12**, 45155–45164.
21 T. Yang, Z. D. Gordon, Y. Li and C. K. Chan, *J. Phys. Chem. C*, 2015, **119**, 14947–14953.
22 J. Fan, T. Wang, Y. Yuan, C.-L. Do-Thanh, X. Suo, Z. Yang, H. Chen and S. Dai, *ACS Appl. Energy Mater.*, 2022, **5**, 3290–3297.
23 T. Wang, J. Fan, C.-L. Do-Thanh, X. Suo, Z. Yang, H. Chen, Y. Yuan, H. Lyu, S. Yang and S. Dai, *Angew. Chem., Int. Ed.*, 2021, **60**, 9953–9958.
24 G. Foran, N. Verdier, D. Lepage, C. Malveau, N. Dupré and M. Dollé, *Polymers*, 2021, **13**, 1207.

25 A. Kuhn, S. Narayanan, L. Spencer, G. Goward, V. Thangadurai and M. Wilkening, *Phys. Rev. B: Condens. Matter Mater. Phys.*, 2011, **83**, 094302.
26 L. van Wüllen, T. Echelmeyer, H.-W. Meyer and D. Wilmer, *Phys. Chem. Chem. Phys.*, 2007, **9**, 3298–3303.
27 T. Thompson, A. Sharafi, M. D. Johannes, A. Huq, J. L. Allen, J. Wolfenstine and J. Sakamoto, *Adv. Energy Mater.*, 2015, **5**, 1500096.
28 D. Wang, G. Zhong, W. K. Pang, Z. Guo, Y. Li, M. J. McDonald, R. Fu, J.-X. Mi and Y. Yang, *Chem. Mater.*, 2015, **27**, 6650–6659.
29 B. Karasulu, S. P. Emge, M. F. Groh, C. P. Grey and A. J. Morris, *J. Am. Chem. Soc.*, 2020, **142**, 3132–3148.
30 Y. Chen, Y. Jiang, S.-S. Chi, H. J. Woo, K. Yu, J. Ma, J. Wang, C. Wang and Y. Deng, *J. Power Sources*, 2022, **521**, 230921.
31 F. Sun, Y. Yang, S. Zhao, Y. Wang, M. Tang, Q. Huang, Y. Ren, H. Su, B. Wang, N. Zhao, X. Guo and H. Yu, *ACS Energy Lett.*, 2022, **7**, 2835–2844.
32 Y. Tian, Y. Zhou, Y. Liu, C. Zhao, W. Wang and Y. Zhou, *Solid State Ionics*, 2020, **354**, 115407.
33 X. Yang, D. Kong, Z. Chen, Y. Sun and Y. Liu, *J. Mater. Sci.: Mater. Electron.*, 2018, **29**, 1523–1529.
34 Y. Zhu, S. Wu, Y. Pan, X. Zhang, Z. Yan and Y. Xiang, *Nanoscale Res. Lett.*, 2020, **15**, 153.
35 S. Aktaş, O. M. Özkendir, Y. R. Eker, Ş. Ateş, Ü. Atav, G. Çelik and W. Klysubun, *J. Alloys Compd.*, 2019, **792**, 279–285.
36 I. Kokal, M. Somer, P. H. L. Notten and H. T. Hintzen, *Solid State Ionics*, 2011, **185**, 42–46.
37 P. J. Kumar, K. Nishimura, M. Senna, A. Düvel, P. Heitjans, T. Kawaguchi, N. Sakamoto, N. Wakiya and H. Suzuki, *RSC Adv.*, 2016, **6**, 62656–62667.